Eur. Phys. J. D **19**, 165–181 (2002)
DOI: 10.1140/epjd/e20020069

THE EUROPEAN PHYSICAL JOURNAL D
EDP Sciences
© Società Italiana di Fisica
Springer-Verlag 2002

Scattering of light exotic atoms in excited states

T.S. Jensen[1,2,a] and V.E. Markushin[1]

[1] Paul Scherrer Institute, 5232 Villigen PSI, Switzerland
[2] Institut für Theoretische Physik der Universität Zürich, Winterthurerstrasse 190, 8057 Zürich, Switzerland

Received 4 December 2001 and Received in final form 4 February 2002

Abstract. The differential and total cross-sections for the scattering of muonic, pionic, kaonic and antiprotonic hydrogen in excited states from atomic hydrogen have been calculated for the purpose of atomic cascade calculations. The scattering problem is treated in a fully quantum mechanical framework which takes the energy shifts and, in the case of the hadronic atoms, the widths of the *ns* states into account. The validity of semiclassical approximations is critically examined.

PACS. 34.50.-s Scattering of atoms and molecules – 36.10.-k Exotic atoms and molecules (containing mesons, muons, and other unusual particles)

1 Introduction

Exotic hydrogen-like atoms are formed in highly excited states, when negative particles (μ^-, π^-, K^-...) are stopped in hydrogen. The deexcitation of exotic atoms proceeds *via* many intermediate states until the ground state is reached or a nuclear reaction takes place. Despite a long history of theoretical and experimental studies (see [1–4] and references therein) the kinetics of this atomic cascade is not yet fully understood. The current generation of experiments with exotic hydrogen-like atoms addresses a number of fundamental problems using precision spectroscopy methods, the success of which relies crucially on a better knowledge of the atomic cascade.

In the case of the laser spectroscopy of the Lamb shift in muonic hydrogen [5], the goal is to determine the proton charge radius with an accuracy of 10^{-3} from the energy splitting between the $2s$ and $2p$ states. This will remove the major theoretical obstacle in the precision calculations of the hydrogen Lamb shift, thus extending the limits of the most stringent test of QED in a bound system. The feasibility of this experiment depends on the population and the lifetime of the metastable $2s$ state of μ^-p, and a reliable model of the cascade kinetics is essential for this issue. The experiment on precision spectroscopy of pionic hydrogen [6] is expected to determine the πN scattering length with a precision better than 1% by measuring the nuclear shifts and widths of the K X-ray lines. At this level of precision, the Doppler broadening corrections to the line width become important, and they must be reliably calculated from a cascade model. In the precision spectroscopy of antiprotonic hydrogen [7], the Doppler broadening of the L X-ray lines must be taken into account when the $2p$ nuclear widths are determined from the X-ray line profile.

The kinetics of atomic cascade is described by the master equation involving all significant processes with the exotic atoms (cascade mechanisms). The deexcitation mechanisms include radiative, Auger, and Coulomb processes where the transition energy between states with different principal quantum number n is carried away mainly by photon, electron, and the recoiling particles (including the exotic atom itself), correspondingly. While the deexcitation processes are obviously essential for the atomic cascade, the role of the collisional processes preserving the principal quantum number n is not less important than that of the deexcitation. The Stark transitions $nl \to nl'$ ($l' \neq l$), affect the population of the nl sublevels. Together with the elastic scattering $nl \to nl$ they decelerate the exotic atoms thus influencing their energy distribution during the cascade. In hadronic atoms, the role of the Stark mixing is especially important as it results in a strong absorption during the cascade by feeding the ns states which have absorption widths much larger than the states with $l > 0$.

In the literature starting with the paper of Leon and Bethe [1], Stark mixing has often been treated in the semiclassical straight-line-trajectory approximation [1,2,8–11]. Due to the broad use of this relatively simple model it is desirable to know its accuracy in comparison with more advanced and realistic quantum mechanical calculations. By introducing phenomenological tuning parameters in the Stark mixing rates [2–4] one is able to reproduce the measured X-ray yields and other experimental data. However, the ultimate goal of *ab initio* cascade calculations demands more accurate results for the collisional processes.

---

[a] e-mail: `thomas.jensen@psi.ch`

A fully quantum mechanical treatment based on adiabatic potentials was given in [12–15]. However, the shifts and widths of the ns states which become important in the final part of the cascade were not included in this framework. The deceleration and radiative quenching of muonic hydrogen in the metastable $2s$ state were studied in a close-coupling framework in [16]. We reexamined the same problem in [17] avoiding some of the approximations used in [16]. As the close-coupling model can be modified in a straightforward manner to include nuclear absorption in hadronic atoms [18], it is well suited for describing the collisional processes during the atomic cascade.

In this paper, we present a unified treatment of Stark mixing, elastic scattering, and, in the case of hadronic atoms, nuclear absorption during collisions. For the time being, we restrict our calculations to exotic hydrogen-like atoms. The paper is organized as follows. In Section 2 we present the quantum mechanical close-coupling framework used for the calculation of the scattering of x^-p atoms in excited states from atomic hydrogen. The same processes are treated in the semiclassical approximation in Section 3. The results (differential, partial wave and total cross-sections) are discussed in Section 4 and summarized in Section 5.

Unless otherwise stated, atomic units ($\hbar = e = m_e = 1$) are used throughout this paper. The unit of cross-section is $a_0^2 = 2.8 \times 10^{-17}$ cm^2, where $a_0 = \hbar^2/m_e e^2$ is the electron Bohr radius.

2 Close-coupling calculation of the cross-sections

In this section, the close-coupling framework developed in reference [17] for the three-body reaction

$$(x^-p)_{nl} + \mathrm{H} \rightarrow (x^-p)_{nl'} + \mathrm{H} \tag{1}$$

will be generalized to include absorption effects in hadronic atoms. The following notations are used: the negative particle x^- with mass m_x and the proton with mass m_p form an exotic atom with the total mass $M_{xp} = m_x + m_p$ and the reduced mass $\mu_{xp} = m_x m_p / M_{xp}$. The coordinates used in the calculations are explained in Figure 1. The relative orbital angular momentum of x^-p and H is denoted by $\mathbf{L}$, the internal x^-p orbital angular momentum by $\mathbf{l}$, and the total orbital angular momentum by $\mathbf{J} = \mathbf{L} + \mathbf{l}$.

2.1 The effective $x^-p - \mathrm{H}$ interaction

The exotic atom x^-p is described by the Hamiltonian

$$H_{xp} = -\frac{\nabla_r^2}{2\mu_{xp}} - \frac{1}{r} + \Delta V \tag{2}$$

where ΔV includes all effects beyond the standard non-relativistic Coulomb two-body problem: vacuum polarization, finite size effects, and, in case of hadronic atoms, strong interaction between the two particles. For the considered systems, ΔV can be treated as a perturbation resulting in the shift ΔE_{nl} of the Coulomb energy levels:

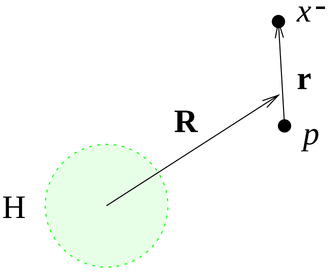

Fig. 1. Coordinates used for the effective three-body system $x^-p - \mathrm{H}$: $\mathbf{R}$ is the vector from the target proton to the center of mass of the exotic atom, $\mathbf{r}$ is the vector from the proton of the x^-p to the x^-. The directions of $\mathbf{R}$ and $\mathbf{r}$ are denoted by Ω and ω, respectively.

$$\langle nlm | H_{xp} | nlm \rangle = E_{nl} = -\frac{\mu_{xp}}{2n^2} + \Delta E_{nl} \tag{3}$$

where the ket $|nlm\rangle$ denotes the nlm state of the standard Coulomb problem. In the case of hadronic atoms, the atomic cascade is often terminated before reaching the ground state due to nuclear reactions like

$$\pi^-p \rightarrow \pi^0 n,\ \gamma n, \tag{4}$$

$$K^-p \rightarrow \Sigma^\pm \pi^\mp, \Sigma^0\pi^0, \Lambda n. \tag{5}$$

This effect is described by the imaginary part of the complex energy shift ΔE_{nl}

$$\mathrm{Im}(\Delta E_{nl}) = -\Gamma_{nl}/2 \tag{6}$$

where the width Γ_{nl} is the nuclear reaction rate from the nl state. For the collisional processes with the exotic hydrogen-like atoms, it is sufficient to take into account only the widths of the ns states. The n dependence of the hadronic part of the complex nuclear shift is described by the Deser formula [19]

$$\Delta E_{ns}^{\mathrm{had}} = \frac{\Delta E_{1s}^{\mathrm{had}}}{n^3} \cdot \tag{7}$$

The Hamiltonian for the $x^-p - \mathrm{H}$ system is given by

$$H = -\frac{\nabla^2}{2\mu} + V(\mathbf{r}, \mathbf{R}) + H_{xp} \tag{8}$$

where

$$\mu = \frac{M_{xp} M_{\mathrm{H}}}{M_{xp} + M_{\mathrm{H}}} \tag{9}$$

is the reduced mass of the $(x^-p + \mathrm{H})$ system, and $V(\mathbf{r}, \mathbf{R})$ is the Coulomb interaction of the exotic atom with the hydrogen electric field. In most cases of cascade studies, the effects of hydrogen excitation or ionization in the collisions without changing n can be neglected. The electric field of a hydrogen atom in the ground state has the form

$$\mathbf{F}(\mathbf{R}) = \frac{\mathbf{R}}{R} F(R) \tag{10}$$

where

$$F(R) = \frac{1}{R^2}(1 + 2R + 2R^2)\mathrm{e}^{-2R}. \tag{11}$$

The potential energy is a function of only three variables

$$V(\mathbf{r}, \mathbf{R}) = V(z', r', R) \tag{12}$$

where $\mathbf{r}' = (x', y', z')$ is $\mathbf{r}$ in a rotated coordinate system with the z'-axis taken along $\mathbf{R}$. The electric field of a hydrogen atom is sufficiently strong to mix the l sublevels of the x^-p atom during a collision at distances of a few atomic units, a_0, which are much larger than the size of the x^-p at low n. Since Stark mixing is essentially a long-distance process, one can use the dipole approximation for the potential

$$V(\mathbf{r}, \mathbf{R}) = z'F(R). \tag{13}$$

This can be easily generalized to scattering from other target atoms: one uses the electric field generated by the nucleus and the electronic charge density.

Given the above defined interactions, we solve the time independent Schrödinger equation

$$H\psi(\mathbf{r}, \mathbf{R}) = E\psi(\mathbf{r}, \mathbf{R}) \tag{14}$$

with the standard boundary conditions for this multichannel scattering problem using the close-coupling approximation. The internal x^-p wave function is expanded into the set of n^2 Coulomb wave functions with the same quantum number n:

$$\psi(\mathbf{r}, \mathbf{R}) = R^{-1} \sum_{JMl\Lambda} \phi_{Jl\Lambda}(R) D^{J*}_{\Lambda M}(\Omega) \chi_{nl\Lambda}(\mathbf{r}'). \tag{15}$$

The functions $\chi_{nl\Lambda}(\mathbf{r}')$ are the Coulomb wave functions in a rotating coordinate system with the z'-axis chosen as the quantization axis and $D^J_{\Lambda M}(\Omega)$ are the corresponding rotation functions (see Appendix A). The functions $\chi_{nl\Lambda}(\mathbf{r}')$ are related to the space fixed functions $\chi_{nlm}(\mathbf{r}) = r_{nl}(r)Y_{lm}(\omega)$ by

$$\chi_{nlm}(\mathbf{r}) = \sum_{\Lambda=-l}^{l} D^{l*}_{m\Lambda}(\Omega)\chi_{nl\Lambda}(\mathbf{r}'). \tag{16}$$

The expansion (15) leads to the set of n^2 coupled second order differential equations for the radial functions $\phi_{Jl\Lambda}(R)$

$$\begin{aligned}\Big(-\frac{1}{2\mu}\frac{\mathrm{d}^2}{\mathrm{d}R^2} + E_{nl} - E\Big)\phi_{Jl\Lambda}(R) \\ + \sum_{l'\Lambda'}\Big(\frac{\langle n; JM\Lambda'l'|\mathbf{L}^2|n; JM\Lambda l\rangle}{2\mu R^2} \\ + {}'\langle nl'\Lambda'|V(z', r', R)|nl\Lambda\rangle'\Big)\phi_{Jl'\Lambda'}(R) = 0.\end{aligned} \tag{17}$$

The basis states $|n; JM\Lambda l\rangle$ are simultaneous eigenstates of H_{xp}, $\mathbf{J}^2$, J_z, $J_{z'}$, and $\mathbf{l}^2$ with eigenvalues E_{nl}, $J(J+1)$, M, Λ, and $l(l+1)$, respectively, and are given by

$$\begin{aligned}|n; JM\Lambda l\rangle &= |JM\Lambda\rangle|nl\Lambda\rangle', \\ \langle\Omega|JM\Lambda\rangle &= \sqrt{\frac{2J+1}{4\pi}} D^{J*}_{M\Lambda}(\Omega), \\ \langle\mathbf{r}'|nl\Lambda\rangle' &= \chi_{nl\Lambda}(\mathbf{r}').\end{aligned} \tag{18}$$

The ket $|nl\Lambda\rangle'$ denotes the eigenstates of the Coulomb problem in the rotated coordinate system.

Because of rotational invariance the quantum numbers J and M are conserved and the radial wavefunctions $\phi_{Jl\Lambda}(R)$ are independent of M. The expansion (15) is convenient for computing matrix elements of the potential $V(z', r', R)$. In the dipole approximation, the nonvanishing matrix elements of z' correspond to $|\Delta l| = 1$ and $\Delta\Lambda = 0$ where one has

$${}'\langle nl\Lambda|z'|n(l-1)\Lambda\rangle' = -\frac{3n}{2\mu_{xp}}\sqrt{\frac{(l^2-\Lambda^2)(n^2-l^2)}{(2l+1)(2l-1)}} \cdot \tag{19}$$

The basis states (18) are not the eigenstates of $\mathbf{L}^2$, but the matrix elements of $\mathbf{L}^2$ can be easily obtained by using

$$\mathbf{L}^2 = (\mathbf{J} - \mathbf{l})^2 = \mathbf{J}^2 + \mathbf{l}^2 - 2J_{z'}l_{z'} - l'_+J'_- - l'_-J'_+ \cdot \tag{20}$$

Together with the results and notations of Appendix A this gives (see also Ref. [20])

$$\begin{aligned}\langle n; JM\Lambda'l'|\mathbf{L}^2|n; JM\Lambda l\rangle = \\ \delta_{ll'}\delta_{\Lambda\Lambda'}\Big(J(J+1) + l(l+1) - 2\Lambda^2\Big) \\ - \delta_{ll'}\Big(\delta_{\Lambda+1\Lambda'}\lambda_-(J,\Lambda)\lambda_+(l,\Lambda) \\ + \delta_{\Lambda-1\Lambda'}\lambda_+(J,\Lambda)\lambda_-(l,\Lambda)\Big).\end{aligned} \tag{21}$$

The rotated basis functions were used by Carboni and Fiorentini [16] to study $(\mu^-p)_{2s} + \mathrm{H}$ collisions in an approximation where the terms $\delta_{ll'}\delta_{\Lambda\Lambda'}(l(l+1)-2\Lambda)$ in equation (21) were neglected.

One can get a partial decoupling of the equations (17) by using the following expansion

$$\psi(\mathbf{r}, \mathbf{R}) = R^{-1}\sum_{JMLl}\xi_{JLl}(R)\mathcal{Y}^{JM}_{Ll}(\Omega, \omega)r_{nl}(r) \tag{22}$$

where the functions

$$\mathcal{Y}^{JM}_{Ll}(\Omega, \omega) = \sum_{M_L m}\langle LlM_Lm|JM\rangle Y_{LM_L}(\Omega)Y_{lm}(\omega) \tag{23}$$

are simultaneous eigenfunctions of $\mathbf{J}^2$, $\mathbf{L}^2$, $\mathbf{l}^2$, and J_z with eigenvalues $J(J+1)$, $L(L+1)$, $l(l+1)$, and M respectively. The system of the radial Schrödinger equations for the functions $\xi_{JLl}(R)$ has the form

$$\begin{aligned}\Big(-\frac{1}{2\mu}\frac{\mathrm{d}^2}{\mathrm{d}R^2} + \frac{L(L+1)}{2\mu R^2} + E_{nl} - E\Big)\xi_{JLl}(R) \\ + \sum_{L'l'}\langle n; L'l'JM|V(z', r', R)|n; LlJM\rangle\xi_{JL'l'}(R) = 0\end{aligned} \tag{24}$$

with the basis states

$$\langle \Omega, \mathbf{r}|n; LlJM\rangle = \mathcal{Y}_{Ll}^{JM}(\Omega,\omega)r_{nl}(r). \qquad (25)$$

Due to the parity conservation, the value $P = (-1)^{L+l}$ is conserved, and, as a result, the n^2 differential equations (24) are decoupled into two sets of $n(n+1)/2$ and $n(n-1)/2$ coupled equations for $P = 1$ and $P = -1$ correspondingly. The systems of equations (17, 24) are related to each other by the linear transformation

$$\phi_{Jl\Lambda}(R) = \sqrt{\frac{2J+1}{4\pi}}\sum_L u_{\Lambda L}^{Jl}\xi_{JlL}(R) \qquad (26)$$

where the coefficients $u_{\Lambda L}^{Jl}$ are given by equation (A.6). The matrix elements of the potential energy can then be obtained from those of the rotated basis by using the coefficients $u_{\Lambda L}^{Jl}$

$$\langle n; L'l'JM|V(z',r',R)|n; LlJM\rangle = \sum_{\Lambda\Lambda'} u_{\Lambda' L'}^{Jl'}u_{\Lambda L}^{Jl}\, {}'\langle nl'\Lambda'|V(z',r',R)|nl\Lambda\rangle' \cdot \qquad (27)$$

2.2 Cross-sections

The scattering matrix was calculated numerically using a version of the variable phase method [21] described in Appendix B. In order to treat the ns states of hadronic atoms as normal asymptotic states the absorptive term (6) was switched off for the distances between x^-p and H larger than $5a_0$. The absorption from the ns states between the collisions can be easily taken into account by means of a cascade model.

The use of the dipole approximation in the quantum mechanical framework makes it necessary to introduce the regularization parameter $R_{\min}$ as explained in Appendix B. The dependence of calculated cross-sections on $R_{\min}$ will show how sensitive the results are to the short distance behavior (we will show a few examples in Sect. 4).

The scattering amplitude for the transition $nlm \rightarrow nl'm'$ is given by

$$f_{nlm\to nl'm'}(\Omega) = \frac{4\pi}{2\mathrm{i}\sqrt{k'k}}\sum_{L'LM'_L}\Big(\mathrm{i}^{L-L'}Y_{L'M'_L}(\Omega) \times \langle n; L'l'M'_Lm'|S-1|n; Ll0m\rangle Y^*_{L0}(0,0)\Big) \qquad (28)$$

where Ω is the CMS scattering angle, k and k' are the CMS relative momenta of the initial and final state correspondingly. The S-matrix elements in (28) are related to the matrix elements between the basis states (18) by the relation

$$\langle n; L'l'M'_Lm'|S|n; Ll0m\rangle = \sum_J \langle L'l'M'_Lm'|Jm\rangle\langle Jm|Ll0m\rangle\langle n; L'l'Jm|S|n; LlJm\rangle \cdot \qquad (29)$$

The differential and total cross-sections for the transitions $nl \rightarrow nl'$ are given by

$$\frac{\mathrm{d}\sigma_{nl\to nl'}}{\mathrm{d}\Omega} = \frac{1}{(2l+1)}\frac{k'}{k}\sum_{m'm}|f_{nlm\to nl'm'}|^2, \qquad (30)$$

$$\begin{aligned}\sigma_{nl\to nl'} &= \frac{1}{(2l+1)}\frac{\pi}{k^2} \times \sum_{JMLL'}|\langle n; L'l'JM|S-1|n; LlJM\rangle|^2\\ &= \frac{1}{(2l+1)}\frac{\pi}{k^2}\sum_J\Big((2J+1) \times \sum_{LL'}|\langle n; L'l'JM|S-1|n; LlJM\rangle|^2\Big). \end{aligned}\qquad (31)$$

The corresponding transport cross-sections are given by

$$\sigma^{\mathrm{tr}}_{nl\to nl'} = \int \mathrm{d}\Omega(1-\cos\theta)\frac{\mathrm{d}\sigma_{nl\to nl'}}{\mathrm{d}\Omega} \cdot \qquad (32)$$

In the case of hadronic atoms, the scattering matrix is not unitary because of the absorption. The cross-sections for the absorption processes are given by

$$\sigma_{nl\to\mathrm{abs}} = \frac{\pi}{k^2}\sum_J\left((2J+1) \times\left(1-\frac{1}{(2l+1)}\sum_{LL'l'}|\langle n; L'l'JM|S|n; LlJM\rangle|^2\right)\right)\cdot \qquad (33)$$

The differential cross-sections (30) and the absorption cross-sections (33) are used in the detailed cascade models as described in [3,4]. When less detailed information is sufficient, l-average cross-sections defined below can be used. In particular, in those cases where the rates for collisions without change in n are much larger than other cascade rates, the approximation of the *statistically weighted* differential cross-section is useful:

$$\frac{\mathrm{d}\sigma_{n-\mathrm{av}}}{\mathrm{d}\Omega} = \frac{1}{n^2}\sum_{ll'}(2l+1)\frac{\mathrm{d}\sigma_{nl\to nl'}}{\mathrm{d}\Omega} \cdot \qquad (34)$$

As a measure of the overall strength of Stark mixing, one can use the l-average Stark cross-section:

$$\sigma_{\mathrm{St}} = \frac{1}{n^2}\sum_{l\neq l'}(2l+1)\sigma_{nl\to nl'}. \qquad (35)$$

For hadronic atoms with the strong absorption in the s states, we define the statistically weighted differential cross-section (34) and the average Stark cross-section (35) to include only terms with $l > 0$ and $l' > 0$. The *average absorption* cross-section is defined by

$$\sigma_{\mathrm{abs}} = \frac{1}{n^2-1}\sum_{l\neq 0}(2l+1)\sigma_{nl\to\mathrm{abs}} \qquad (36)$$

which gives a measure of the absorption strength under the assumption of statistical population of the $l \neq 0$ sublevels. Strong absorption can also take place between the collisions (if the hadronic atom leaves the collision zone in an s state) which is not reflected by equation (36). To this end we define the average cross-section

$$\sigma_{\mathrm{av}\to ns} = \frac{1}{n^2-1}\sum_{l\neq 0}(2l+1)\sigma_{nl\to ns} \tag{37}$$

which describes the transitions to the ns state from the statistically populated nl sublevels with $l > 0$. Whether the s state is completely or partially depleted between the collisions depends on the type of atom, the quantum number n, the density of the target, and the kinetic energy. To estimate the upper limit of the absorption, we define the *maximum absorption* cross-section as the l-averaged sum of the cross-sections for nuclear absorption during and after collision

$$\sigma_{\mathrm{max\ abs}} = \sigma_{\mathrm{abs}} + \sigma_{\mathrm{av}\to ns}. \tag{38}$$

The Stark mixing, deceleration, and absorption rates, which are often used in cascade calculations, are defined by the formulas

$$\lambda_{\mathrm{St}} = Nv\sigma_{\mathrm{St}}, \tag{39}$$

$$\lambda_{\mathrm{dec}} = 2\frac{M_{\mathrm{H}}M_{xp}}{(M_{\mathrm{H}}+M_{xp})^2}Nv\sigma_{\mathrm{tr}}, \tag{40}$$

$$\lambda_{\mathrm{abs}} = Nv\sigma_{\mathrm{abs}} \tag{41}$$

where N is the target density and v the velocity of the exotic atom. When a significant part of the nuclear reactions takes place between the collisions, the absorption is better described by the *effective absorption rate* defined as following

$$\lambda_{\mathrm{eff\ abs}} = \lambda_{\mathrm{abs}} + \frac{\lambda_{\mathrm{av}\to ns}}{1+\sum_{l\neq 0}\lambda_{ns\to nl}/\Gamma_{ns}}\cdot \tag{42}$$

In the case of very strong absorption during the collisions, the relation $\lambda_{\mathrm{av}\to ns} \ll \lambda_{\mathrm{abs}}$ holds, and therefore

$$\lambda_{\mathrm{eff\ abs}} \approx \lambda_{\mathrm{abs}} \qquad (\text{for } \Gamma_{ns}\to\infty)\cdot \tag{43}$$

When absorption from the p states is important, the effective rate for p state absorption is defined analogously to equation (42) by considering statistically populated $l > 1$ states. A simple comparison of the energy dependent rates for the different processes cannot substitute detailed cascade calculations using the detailed cross-sections equations (30, 33) but may be helpful for getting a quick overview. We shall present a few examples in Section 4.

3 Semiclassical approximation

As the number of coupled second order differential equations in the quantum mechanical model of Section 2 grows as n^2, a simpler framework is desirable for high n states. If the collision energy is sufficiently large, one can expect that the relative x^-p – H motion can be treated classically. A rough estimate of the minimum kinetic energy T for which a classical-trajectory description is valid can be obtained from the requirement that a large number of partial waves $L \sim 2a_0k$ ($2a_0$ being the approximate range of the interaction) contribute to the cross-section; that gives for the kinetic energy of muonic hydrogen $T > 0.7$ eV at $L > 10$. As known from experiment (see [4] and references therein), the exotic atoms can reach kinetic energies of several eV during the cascade, and this makes a semiclassical treatment applicable to many cases of practical interest. The model that has been used most often is the straight-line-trajectory approximation [1,2,8–11] where the small neutral exotic atom is considered as moving along a straight line with constant velocity through the electric field of the target atom[1]. The time dependent electric field causes transitions among the sublevels of the exotic atom, which are treated quantum mechanically. This approach was usually used for the calculation of the Stark mixing rates, but, as discussed below, differential and absorption cross-sections can be calculated as well.

A semiclassical description of our scattering problem is obtained by treating some of the 6 variables (**R** and **r**) as classical time dependent variables. The remaining variables correspond to the quantum mechanical part of the system that is described by the wave function $\psi(t)$ satisfying the Schrödinger equation

$$\mathrm{i}\frac{\partial\psi(t)}{\partial t} = H^{\mathrm{SC}}(t)\psi(t) \tag{44}$$

where $H^{\mathrm{SC}}(t)$ depends on t through the classical variables. The wave function $\psi(t)$ is expanded into a set of orthonormal basis states

$$\psi(t) = \sum_j a_j(t)|\alpha_j\rangle \tag{45}$$

leading to the time dependent Schrödinger equation

$$\mathrm{i}\dot{a}_j(t) = \sum_k H^{\mathrm{SC}}_{jk}(t)a_k(t) \tag{46}$$

which must be solved with appropriate boundary conditions.

To establish a connection to results in the literature we will first discuss the simple fixed field model of Leon and Bethe [1,11] where the **R** motion is assumed to be classical and the x^-p atom is treated quantum mechanically. The assumptions are as follows: the x^-p moves along a straight line with constant velocity v ($R(t) = \sqrt{(vt)^2+\rho^2}$ where ρ is the impact parameter), only transitions within the n^2 states with the given principal quantum number n are considered, all the n^2 states are degenerate, and the electric field from the target atom is directed along the

---

[1] Another possibility, which we will not consider here, is to use deflected trajectories.

quantization axis of the x^-p. After expanding the internal wave function of the exotic atom into the Stark eigenstates ($|nn_1\Lambda\rangle$, $n_1 = 0, ..., n - |\Lambda| - 1$) one is left with a single channel scattering problem

$$\mathrm{i}\dot{a}_{nn_1\Lambda}(t) = V_{nn_1\Lambda}(R(t))a_{nn_1\Lambda}(t) \tag{47}$$

where

$$V_{nn_1\Lambda}(R) = \frac{3n}{2\mu_{xp}}(2n_1 - n + |\Lambda| + 1)F(R). \tag{48}$$

Equation (47) is solved with the boundary condition

$$a_{nn_1\Lambda}(-\infty) = 1 \tag{49}$$

for a range of values of the impact parameter ρ

$$a_{nn_1\Lambda}(t) = \exp\left(-\mathrm{i}\int_{\infty}^{t} V(R(t))\mathrm{d}t\right)\cdot \tag{50}$$

The eikonal phase shift function [22]

$$\chi(\rho) = -\int_{\infty}^{\infty} V(R(t))\mathrm{d}t \tag{51}$$

is used (we take $J+1/2 = k\rho$, where $k = \mu v$ is the relative momentum) to obtain the scattering amplitude

$$f^{\text{eikonal}}_{nn_1\Lambda}(\theta) = \frac{1}{2\mathrm{i}k}\sum_{J=0}^{J_{\max}}(2J+1) \times (\mathrm{e}^{\mathrm{i}\chi((J+1/2)/k)} - 1)P_J(\cos\theta) \tag{52}$$

and the differential cross-sections

$$\frac{\mathrm{d}\sigma^{\text{eikonal}}_{nn_1\Lambda}}{\mathrm{d}\Omega} = |f^{\text{eikonal}}_{nn_1\Lambda}(\theta)|^2. \tag{53}$$

This model is not sufficiently accurate for our purposes. In Section 3.1 we generalize it to include different thresholds, nuclear absorption during collisions, and correct angular coupling between the substates.

3.1 Semiclassical model

In this case only the radial R motion is considered to be classical, the other five variables (Ω, $\mathbf{r}$) are kept quantized. The problem of x^-p scattering from hydrogen becomes a multichannel scattering problem with different channel momenta and orbital angular momenta. We collect the (complex) energy shifts and the angular part of the kinetic energy of the different channels in the diagonal $n^2 \times n^2$ matrices ΔE and L, respectively. The collision is specified by the CMS collision energy

$$E_{\text{cm}} = \frac{1}{2}\mu v^2 = \frac{k^2}{2\mu} \tag{54}$$

and the angular momentum J. Neglecting the deflection of the neutral x^-p atom we take the classical motion to be

$$R = R(t) = \sqrt{(vt)^2 + \rho^2} \tag{55}$$

where $\rho = \sqrt{J(J+1)}/k$. This introduces some ambiguity into the model because it requires a common motion $R(t)$ for all channels. In this paper we take the common momentum k to be that of the $l = (n-1)$ states for hadronic atoms while we use the ns state in the case of muonic hydrogen.

We expand the quantum mechanical part of the system into the states

$$|\alpha_j\rangle = |n; LlJM\rangle \tag{56}$$

and obtain the time dependent Schrödinger equation in matrix form

$$\mathrm{i}\dot{A}(t) = H^{\text{SC}}(t)A(t) \tag{57}$$

where $H^{\text{SC}}(t)$ is a $n^2 \times n^2$ matrix given by

$$H^{\text{SC}}(t) = \frac{L(L+1) - J(J+1)}{2\mu R^2(t)} + V(R(t)) + \Delta E. \tag{58}$$

The potential matrix has the elements

$$V_{ij}(R) = \langle n; L'l'JM|V|n; LlJM\rangle \tag{59}$$

as in equation (24).

Equations (57) are integrated from $-t_{\max}$ to $t_{\max}$, where $t_{\max}$ is chosen so large that the potential can be neglected for distances larger than $R(t_{\max})$, with the boundary conditions

$$A(-t_{\max}) = I. \tag{60}$$

The semiclassical scattering matrix is given by

$$S^{\text{SC}} = QA(t_{\max})Q \tag{61}$$

where Q is the diagonal matrix given by

$$Q = \exp\Big(\mathrm{i}\frac{L(L+1) - J(J+1)}{2\rho k}\arctan(vt_{\max}/\rho) + \mathrm{i}\mathrm{Re}(\Delta E)t_{\max}\Big). \tag{62}$$

With the semiclassical scattering matrix and the formulas from Section 2, results for differential, total and absorption cross-sections can be obtained.

3.2 Fixed field model

The semiclassical approximation simplifies the numerical calculations: instead of a system of second order differential equations the same number of first order differential equations must be solved. A further simplification can be made by neglecting the coupling between the internal x^-p angular momentum $\mathbf{l}$ and the orbital angular momentum $\mathbf{L}$. This corresponds to the approximation

$$L = J \tag{63}$$

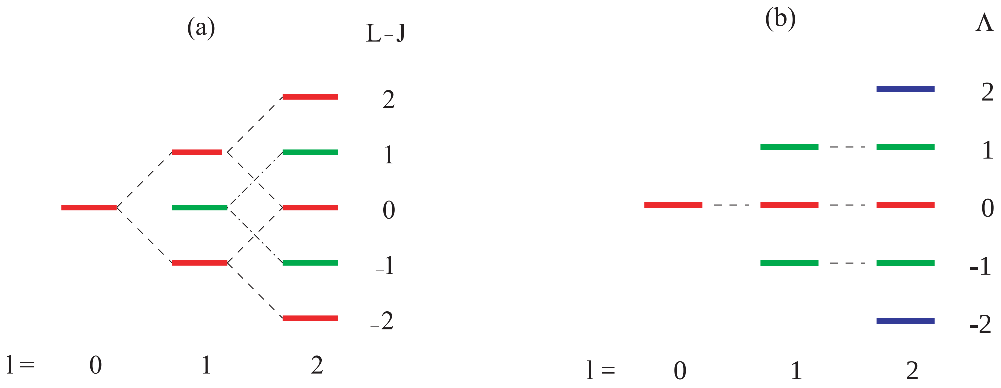

Fig. 2. Coupling between the sublevels in an $x^-p-\mathrm{H}$ collision. The correct coupling (a) conserves parity. In the fixed field model (b) transitions are only possible between states with the same eigenvalue Λ of x^-p angular momentum along the interatomic axis.

in the case discussed above in Section 3.1. In this approximation, the quantum number Λ is conserved in addition to J and M (see Fig. 2).

By expanding the solution into the rotated basis states ($|\alpha_j\rangle = |n; JM\Lambda l\rangle$) one finds the time dependent Schrödinger equation in matrix form

$$\mathrm{i}\dot{A}(t) = (ZF(R(t)) + \Delta E)\, A(t), \tag{64}$$
$$A(-t_{\max}) = I \tag{65}$$

where

$$Z_{ij} = {}'\langle nl\Lambda|z'|nl'\Lambda\rangle' \cdot \tag{66}$$

Equation (64) must be solved for each value of Λ, $|\Lambda| < n$. If the states with $l > 0$ are taken to be degenerate, equation (64) with $\Lambda \neq 0$ decouple completely in parabolic coordinates [1,11] and is easily integrated as shown above. This is also the case for $\Lambda = 0$ when the ns energy shift is negligible. If not, one must solve n coupled first order equations.

The fixed field scattering matrix is defined by

$$S^{\mathrm{FF}} = Q^{\mathrm{FF}} A(t_{\max}) Q^{\mathrm{FF}} \tag{67}$$

where the diagonal matrix Q^{FF} is given by

$$Q^{\mathrm{FF}} = \exp\Big(\mathrm{i}\mathrm{Re}(\Delta E) t_{\max}\Big) \cdot \tag{68}$$

The fixed field scattering amplitude is given by

$$f_{nl\Lambda\to nl'\Lambda}(\theta) = \frac{1}{2\mathrm{i}k} \times \sum_J (2J+1)\langle n; JM\Lambda l'|S^{\mathrm{FF}} - 1|n; JM\Lambda l\rangle P_J(\cos\theta) \tag{69}$$

and the differential cross-section by

$$\frac{\mathrm{d}\sigma_{nl\to nl'}}{\mathrm{d}\Omega} = \frac{1}{2l+1}\sum_\Lambda |f_{nl\Lambda\to nl'\Lambda}(\theta)|^2. \tag{70}$$

The matrix elements in the r.h.s of equation (69) are actually independent of M since this quantum number is conserved. The cross-sections for the processes $nl \to nl'$ and $nl \to$ absorption are given by

$$\sigma_{nl\to nl'} = \frac{1}{2l+1}\frac{\pi}{k^2} \times \sum_J (2J+1) \sum_\Lambda |\langle n; JM\Lambda l'|S^{\mathrm{FF}} - 1|n; JM\Lambda l\rangle|^2 \tag{71}$$

and

$$\sigma_{nl\to \mathrm{abs}} = \frac{1}{2l+1}\frac{\pi}{k^2}\sum_J (2J+1)\Big((2l+1) - \sum_{\Lambda l'} |\langle n; JM\Lambda l'|S^{\mathrm{FF}}|n; JM\Lambda l\rangle|^2\Big) \cdot \tag{72}$$

4 Results

Using the methods described in Sections 2 and 3 we have calculated the cross-sections for the collisions of the μ^-p, π^-p, K^-p, and $\bar{p}p$ atoms in excited states with hydrogen atoms. Our calculations had two major goals: first, to provide comprehensive sets of the collisional cross-sections, which are necessary for detailed cascade calculations, and, second, to investigate the range of validity of the approximate methods based on the semiclassical model and often used in the literature. The numerical calculations have been done for the principal quantum numbers n and the atomic kinetic energies that are of interest for the cascade calculations. The quantum mechanical framework of Section 2 was used for the lower excited states $n = 2$–5, and the semiclassical calculations were done for the range of n up to $n \sim 10$.

As the number of the calculated differential cross-sections is quite large (about 1 200 for μ^-p) only a small part of the results can be shown here, as we describe some main features of the calculated cross-sections illustrating them with particular examples for different exotic atoms. Concerning the detailed results, they have all been used

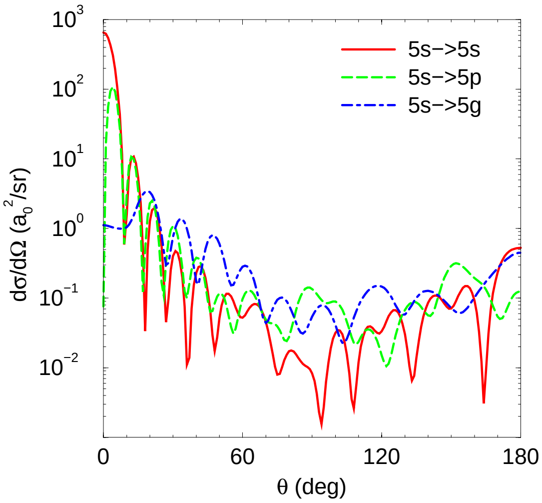

Fig. 3. The differential cross-sections for $(\mu^- p)_{5s} + \mathrm{H} \rightarrow (\mu^- p)_{5s,p,g} + \mathrm{H}$ *vs.* CMS scattering angle θ at the laboratory kinetic energy $T = 3$ eV.

as input for the Monte Carlo kinetics code [23,24], and the results of the cascade calculations will be published elsewhere.

4.1 Muonic hydrogen

The muonic hydrogen scattering is the least complicated case because there is no nuclear absorption in the interaction. The differential cross-sections are known to have a characteristic shape with a strong forward peak and a pattern of maxima and minima [14,17,18] as expected for the interaction that is essentially of a dipole-like type. Figure 3 shows an example of the differential cross-sections for the elastic scattering $5s \rightarrow 5s$ and Stark transitions $5s \rightarrow 5p$ and $5s \rightarrow 5g$. The elastic cross-section has a strong peak at zero scattering angle, while the Stark transitions reach their maxima at finite scattering angle. The peaking in the forward hemisphere is much less pronounced for larger changes in quantum number l.

To compare the results of different methods from the viewpoint of practical applications it is better to look at cross-sections averaged over some appropriate distribution over l or kinetic energy T since many tiny details will be washed out anyway in the cascade evolution. For the purpose of illustration as well as for simple estimates, the statistically weighted cross-sections are especially useful. Figure 4 shows an example of the statistically weighted differential cross-section for $n = 5$ calculated in the fully quantum mechanical model for two values of the cut-off parameter R_{min} (0.05 and 0.10) in comparison with the semiclassical and fixed field approximation. While the cross-sections for the individual transitions $nl \rightarrow nl'$ are somewhat sensitive to the short range cut off R_{min}, the cut-off dependence smoothes out in the averaged cross-sections. The semiclassical results are in a good agreement with the quantum mechanical ones for energies above 1 eV and $n > 2$. The fixed field model provides, on average, a fair agreement with the more accurate methods for the scattering.

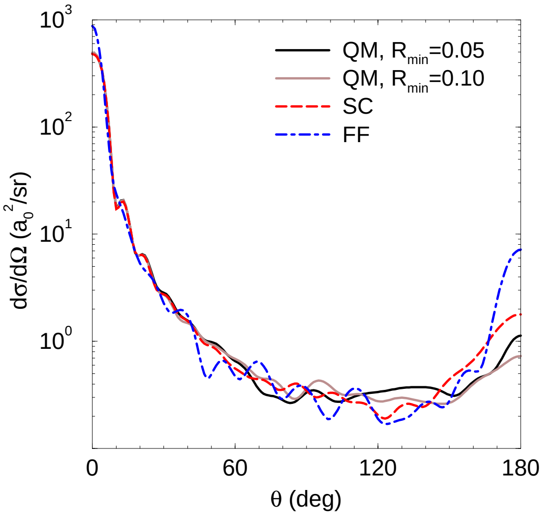

Fig. 4. The statistically weighted differential cross-sections for $(\mu^- p)_{n=5} + \mathrm{H} \rightarrow (\mu^- p)_{n=5} + \mathrm{H}$ *vs.* CMS scattering angle θ at the laboratory kinetic energy $T = 3$ eV. The fully quantum mechanical (QM) results computed with $R_{\mathrm{min}} = 0.05$ and 0.10 are shown with solid lines, the result of the semiclassical (SC) model is shown with a dashed line, and that of the fixed field model (FF) with a dash-dotted line.

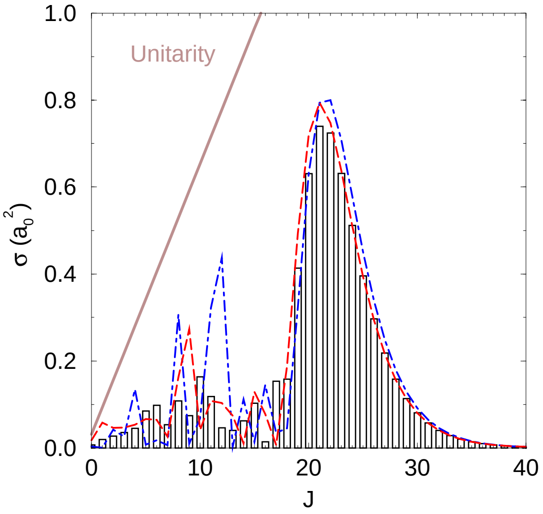

Fig. 5. Partial wave cross-sections for $(\mu^- p)_{5s} + \mathrm{H} \rightarrow (\mu^- p)_{5p} + \mathrm{H}$ *vs.* total angular momentum J at the laboratory kinetic energy $T = 3$ eV. The fully quantum mechanical results are shown with bars, the dashed and dash-dotted lines correspond to the semiclassical and the fixed field models.

Another illuminating way to inspect the complicated structure of the differential cross-sections is presented in Figure 5 that shows the partial wave cross-sections for the reaction $(\mu^- p)_{5s} + \mathrm{H} \rightarrow (\mu^- p)_{5p} + \mathrm{H}$ at $T = 3$ eV. The partial waves can be divided in two groups corresponding to the regimes of "weak-coupling" or "strong-coupling" behavior. The higher partial waves can be reliably described ($J \geq ka \approx 18$ for this example) in the semiclassical

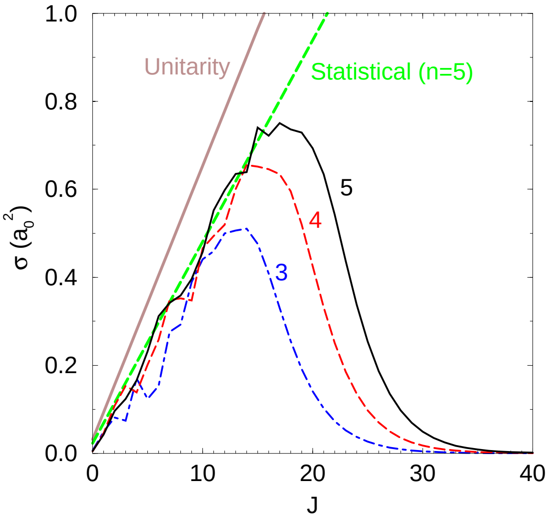

Fig. 6. Total angular momentum dependence of the average Stark cross-sections for $n = 3, 4, 5$ at the laboratory kinetic energy $T = 3$ eV. The light solid line is the unitarity limit, and the light dashed line is the result for the statistical mixing.

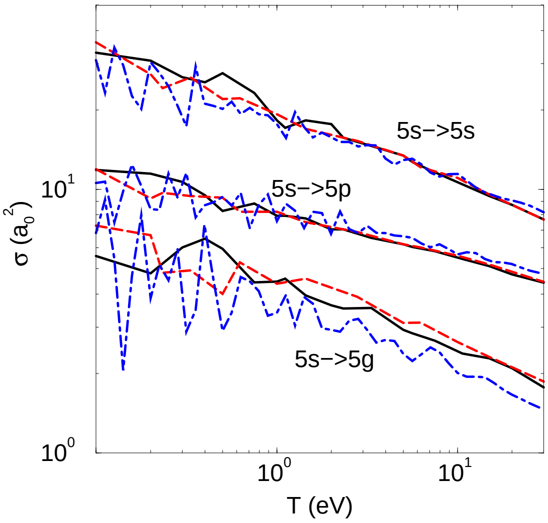

Fig. 7. Cross-sections for $(\mu^-p)_{5s} + \mathrm{H} \to (\mu^-p)_{5s,p,g} + \mathrm{H}$ *vs.* laboratory kinetic energy T. The fully quantum mechanical results (solid lines) are shown in comparison with the results of the semiclassical (dashed lines) and the the fixed field model (dash-dotted lines).

approximation, with the partial cross-section showing a smooth dependence on the total angular momentum J.

For the lower partial waves, all l states are strongly mixed with each other, and the partial cross-sections display a strong dependence on both J and T. While the semiclassical approximation is not applicable in this situation for individual amplitudes, it still makes a reasonable estimate for the average partial cross-sections as they are mainly determined by the statistical weight of the final states. As long as the largest contribution to the total cross-section comes from the total angular momenta corresponding to the semiclassical regime, the semiclassical approximation is adequate for all practical purposes. These two regions of J are also different with respect to the dependence of the Stark cross-sections on the change of the orbital quantum number l. In the semiclassical regime, the transition amplitude rapidly decreases with increasing change in l. In particular, the corresponding partial cross-sections for the transition $5s \to 5p$ are larger than the ones for the $5s \to 5d$ transition.

Figure 6 shows the statistical average partial cross-sections for Stark mixing in the states $n = 3, 4, 5$ in comparison with the unitarity limit. In the strong coupling regime, a simple estimate for the average cross-section can be obtained by assuming that the scattering phases are rapidly changing, so that they appear as being "random" (in the old picture of the Stark phase accumulated along a trajectory with a small impact parameter it corresponds to the so-called complete mixing when the initial state is forgotten after the collision). For the higher partial waves, the average cross-sections are limited not by the unitarity constraint, but by the centrifugal barrier which becomes so strong that it prevents the exotic atom from getting close to the hydrogen atom.

The dependence of the total cross-sections on the kinetic energy is shown in Figure 7 for the transitions with different change in the μ^-p orbital quantum number $l_f - l_i = 0, 1, 4$: $(\mu^-p)_{5s} + \mathrm{H} \to (\mu^-p)_{5s,p,g} + \mathrm{H}$. As it was said before, the semiclassical calculations are in a good agreement with the quantum mechanical ones for kinetic energies above 1 eV. Below 1 eV, where only a few partial waves contribute, the agreement is still fair after averaging over some energy range. The fixed field model is in a fair agreement with the other two. The cross-sections of the fixed field model tend to oscillate more than the cross-sections computed in the other two models. For example, in the fixed field model the $5s$ state is coupled only to one of the $5g$ substates and the corresponding transition is described by one phase shift for each partial wave J. The quantum mechanical and the semiclassical models connect the $5s$ state with 5 of the 9 substates $5g$ (see Fig. 2) for a given angular momentum J, and the average cross-section is smoother as it is distributed over a larger number of individual contributions. Compared to the $5s \to 5p$ cross-section, the fluctuations in the $5s \to 5g$ cross section in the fixed field approximation are stronger because fewer partial waves contribute to this transition.

A brief overview of the Stark mixing and the deceleration in competition with the deexcitation mechanisms is presented in Figure 8 for a typical example of the μ^-p state $n = 5$ in hydrogen gas at 15 bar corresponding to 0.018 of liquid hydrogen density. The muonic hydrogen atoms arriving at the $n = 5$ state during the atomic cascade will, on average, undergo a few transitions changing the orbital quantum number and loose about half of their kinetic energy before Auger deexcitation or, less probably, the radiative transition takes place (assuming no other effects, like muonic molecule formation). Because the evolution of the kinetic energy distribution is important, detailed kinetics cascade calculations [23,24] are needed to treat this problem.

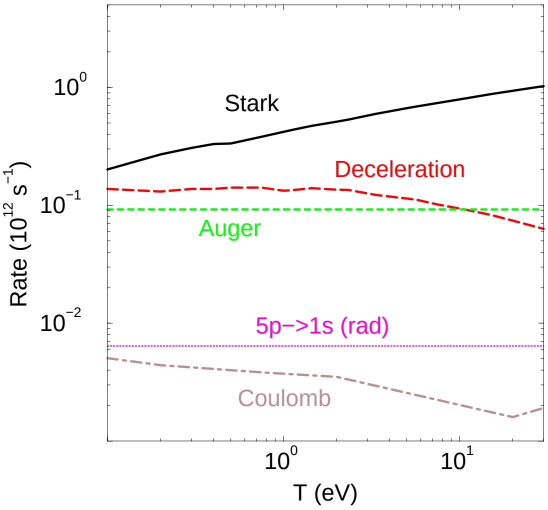

Fig. 8. The energy dependence of the l-average Stark (solid line) and deceleration (dashed line) rates for $(\mu^- p)_{n=5}$ at 15 bar in comparison with the radiative $5p \to 1s$ rate (dotted line), the rates for $n = 5 \to 4$ external Auger effect [1] (light short-dashed line) and the $n = 5 \to 4$ Coulomb deexcitation [25] (light dash-dotted line).

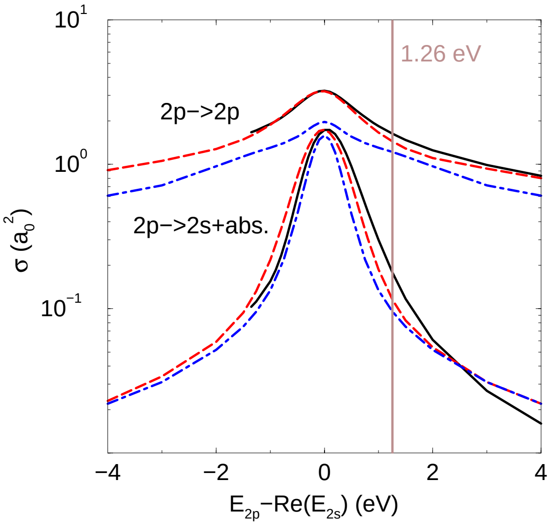

Fig. 9. The pionic hydrogen cross-sections for the elastic scattering $2p \to 2p$ and the maximum absorption from the $2p$ state *vs.* the $2p - 2s$ energy difference at the laboratory kinetic energy $T = 3$ eV. The fully quantum mechanical results are shown with solid lines. The semiclassical results are shown with dashed lines and those of the fixed field model with dash-dotted lines. The light vertical line shows the physical value for the energy splitting. The $2s$ width is $\Gamma_{2s} = 0.11$ eV.

4.2 Pionic hydrogen

The scattering problem for hadronic atoms is more complicated than for the muonic atoms because of the nuclear absorption and larger energy shifts. The previous fully quantum mechanical calculations based on adiabatic potentials [14,15] did not take the shifts and widths of the s states into account, and all the other studies were based either on the approximation suggested in [1] or on the time dependent Stark mixing along classical trajectories [26,27]. In this section we present the first results of the quantum mechanical calculations in comparison with the traditional approximations. The strong interaction shift and width of the $1s$ state of pionic hydrogen from the final analysis of the PSI experiment [28,29] were used to calculate the complex energy shifts of the ns states:

$$\Delta E_{ns} = \frac{\epsilon_{1s}^{\mathrm{had}} - \mathrm{i}\Gamma_{1s}/2}{n^3} + \epsilon_{ns}^{\mathrm{vp}}, \tag{73}$$

$$\epsilon_{1s}^{\mathrm{had}} = -7.11\ \mathrm{eV}, \tag{74}$$

$$\Gamma_{1s} = 0.87\ \mathrm{eV} \tag{75}$$

where $\epsilon_{ns}^{\mathrm{vp}}$ is the energy shift due to the vacuum polarization [30]

$$\epsilon_{1s}^{\mathrm{vp}} = -3.24\ \mathrm{eV}, \tag{76}$$

$$\epsilon_{2s}^{\mathrm{vp}} = -0.37\ \mathrm{eV}, \tag{77}$$

$$\epsilon_{3s}^{\mathrm{vp}} = -0.11\ \mathrm{eV}. \tag{78}$$

The collisions with transitions between the states $l > 0$ $(n > 2)$ are qualitatively similar to muonic hydrogen with respect to Stark mixing and differential cross-sections. The transitions to the ns states are less probable due to the strong interaction energy shift and the nuclear reactions taking place during collisions.

To illustrate the effect of the complex energy shift we consider the cross-sections $\sigma_{2p\to 2p}$ and the maximum absorption cross-section $\sigma_{\mathrm{max\ abs}} = \sigma_{2p\to\mathrm{abs}} + \sigma_{2p\to 2s}$ at $T = 3$ eV for different unphysical values of the $2p - 2s$ energy difference and the widths Γ_{2s} using the models described in Sections 2 and 3. Figure 9 shows the dependence on the energy shift for the physical value of the width $\Gamma_{2s} = 0.11$ eV. All three models feature a strong influence of the energy splitting $|E_{2p} - \mathrm{Re}(E_{2s})|$ on the Stark mixing with the $2s$ state: the nuclear absorption is much more likely when the energy splitting is small in comparison with the characteristic Stark splitting in the electric field of the target atom. For small $|E_{2p} - \mathrm{Re}(E_{2s})|$, the semiclassical model agrees well with the quantum mechanical results for both cross-sections, but starts to deviate when the energy splitting is increased.

The dependence of the cross-sections on the Γ_{2s} with the energy difference fixed at the physical value 1.26 eV (the sum of the strong interaction shift and the vacuum polarization) is shown in Figure 10. For $\Gamma_{2s} > 0.5$ eV, the absorption cross-sections calculated in the semiclassical model are in good agreement with the quantum mechanical result, while the result of the fixed field model is about 20% lower. The good agreement between the semiclassical and the quantum mechanical model can be explained as follows: when the nuclear reaction rate is high the absorption process takes place immediately from a mixed $2s - 2p$ state and is not very sensitive to the kinematics of the $2s$ channel (the available phase space), which is treated incorrectly in the semiclassical approximation. Both the semiclassical and the fixed field models break

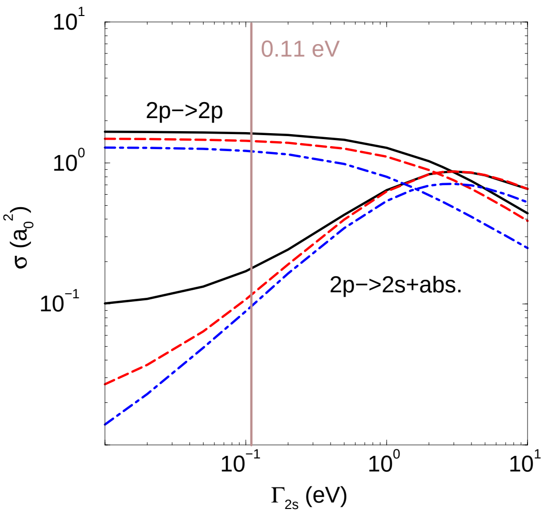

Fig. 10. The pionic hydrogen cross-sections for the elastic scattering $2p \longrightarrow 2p$ and maximum absorption from the $2p$ state *vs.* the nuclear width Γ_{2s} at the laboratory kinetic energy $T = 3$ eV. The fully quantum mechanical results are shown with solid lines. The semiclassical results are shown with dashed lines and those of the fixed field model with dash-dotted lines. The light vertical line shows the physical value for the $2s$ width. The $2p - 2s$ energy splitting is 1.26 eV.

down for smaller Γ_{2s}, including the physical value, where an accurate treatment of the kinematics is necessary.

In general, the fixed field model underestimates the nuclear absorption during collision in comparison with the semiclassical model. As shown in Figure 2, the fixed field model allows only one of the $2p$ substates to be mixed with the $2s$ state and undergo nuclear absorption, whereas the correct parity conserving angular coupling used in our semiclassical model mixes two of the $2p$ substates with the $2s$ state (in the coupled basis). For example, for the physical values ($E_{2p} - \mathrm{Re}(E_{2s}) = 1.26$ eV and $\Gamma_{2s} = 0.11$ eV) the maximum absorption cross-section at 3 eV is increased by about 18% when the semiclassical model is used instead of the fixed field model.

In our quantum mechanical model, the interaction between the exotic atom and the target hydrogen atom is approximated by the dipole term, which is adequate for large distances. When the distance becomes small, this approximation breaks down together with the other ones (the close-coupling expansion into the basis of atomic states with the same n without taking into account symmetry requirements for identical particles). Neglecting rotational coupling and energy shifts, the effective potential energy in the dipole approximation for $\pi^- p$−H system is given by

$$V_{\mathrm{eff}}(R) = \frac{3n}{2\mu_{\pi^- p}}(2n_1 - n + |\Lambda| + 1)F(R) + \frac{J(J+1)}{2\mu R^2} \tag{79}$$

where the parabolic quantum number n_1 runs from 0 to $n - |\Lambda| - 1$. Figure 11 shows $V_{\mathrm{eff}}(R)$ as a function of R for $n = 3$ and $J = 4$. Three of the nine potentials are attractive for small R and have a R^{-2} singularity in $R = 0$. The corresponding phase shifts are ill-defined in these cases. When the correct angular coupling is used and the energy shifts are included, the potential curves are modified, but the problem with the ill-defined phase shifts in the dipole approximation remains. In the present model, the problem is cured by inserting an infinitely hard sphere with radius R_{min} around the target nucleus. For low angular momentum, this introduces a dependence of the scattering matrix on the cut-off parameter R_{min}. This should be considered as an uncertainty of the model related to the approximate treatment of the short distance behavior. An example of the R_{min} dependence in the calculation of the $(\pi^- p)_{n=3} + H$ scattering is shown in Figure 12 for the l-average ($l > 0$) Stark, transport, and maximum absorption cross-sections. Both the Stark and the absorption cross-sections are rather insensitive to the

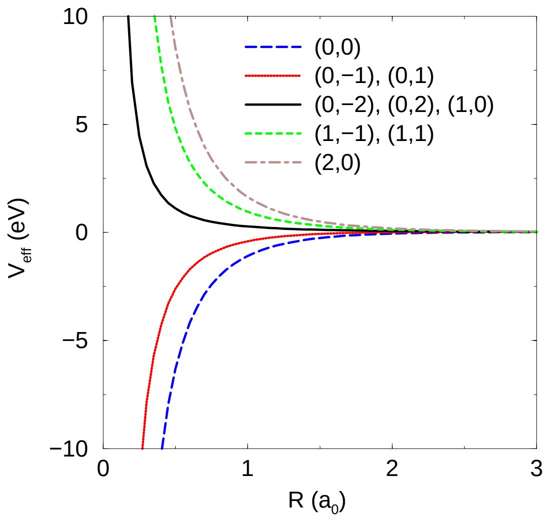

Fig. 11. The effective potentials for the system $(\pi^- p)_{n=3} + \mathrm{H}$ with total angular momentum $J = 4$. The curves are labeled with the quantum numbers (n_1, Λ).

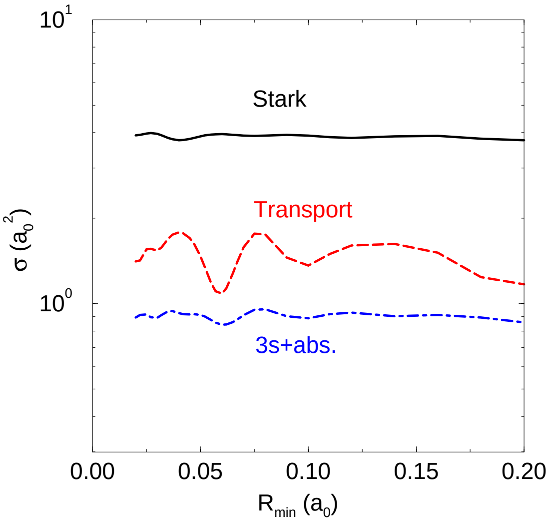

Fig. 12. l-average Stark, transport, and maximum absorption cross-sections for $(\pi^- p)_{n=3} + \mathrm{H}$ scattering *vs.* short distance cut-off R_{min}. The laboratory kinetic energy is 3 eV.

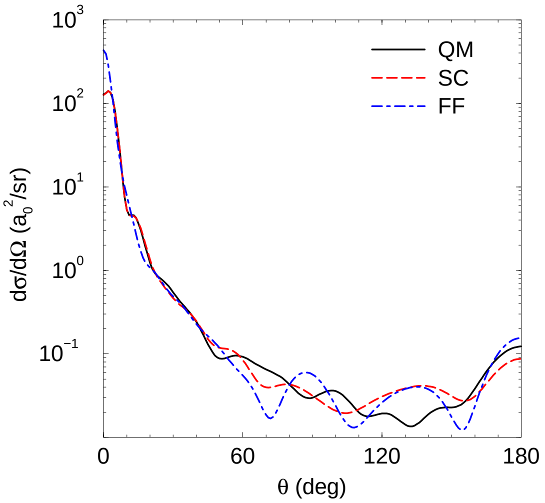

Fig. 13. Statistically weighted differential cross-sections for the $(\pi^-p)_{n=3}+\mathrm{H}$ scattering *vs.* CMS scattering angle θ at the laboratory kinetic energy $T = 10$ eV. The solid line is the fully quantum mechanical result, the dashed line is the semiclassical model, and the dash-dotted line is fixed field model.

value of $R_{\min}$, whereas the transport cross-section, which is more sensitive to the low partial waves, varies moderately ($1.0{-}1.8a_0^2$). However, this dependence of the transport cross-section is less significant when the energy distribution in the atomic cascade is taken into account.

The statistically weighted differential cross-sections for the $l > 0$ sector for $(\pi^-p)_{n=3}+H$ scattering shown in Figure 13 have the similar shape as those of the corresponding process for $n = 5$ in muonic hydrogen (Fig. 4). Both the semiclassical and the fixed field model work well at kinetic energy $T > 1$ eV.

The J dependence of the average Stark cross-section (only the states $l > 0$ are included) and the maximum absorption cross-sections (the sum of the absorption during collision and $3p, 3d \to 3s$) at kinetic energy 10 eV is shown in Figure 14. Like in the case of muonic hydrogen, the contribution to the Stark cross-section can be divided into two parts: a small J region, where the mixing is strong and the distribution over the final states is approximately statistical, and a large J region, where the transitions with $|\Delta l| = 1$ dominate. The semiclassical model is in a good agreement with the quantum mechanical model, whereas the agreement with the fixed field model is fair. All three models are in a fair agreement for the maximum absorption cross-sections.

The relative role of nuclear absorption during the collisions and between the collisions is illustrated in Figure 15 for pionic hydrogen with $n = 3$. The absorption cross-section (*i.e.* the cross-section for nuclear absorption during the collision, Eq. (36)) is shown in comparison with the maximum absorption cross-section, equation (38). For energies larger than ~ 2 eV the π^-p atom is more likely to leave the collision zone in the $3s$ state than undergo nuclear absorption. At high density, many of the $(\pi^-p)_{3s}$ atoms with high kinetic energy will leave the $3s$ state before the nuclear reaction can take place. The results of the semiclassical and the fixed field model are in a good agreement with the quantum mechanical results for kinetic energies larger than 10 eV. Below 10 eV the semiclassical description breaks down and significantly underestimates the absorption cross-sections.

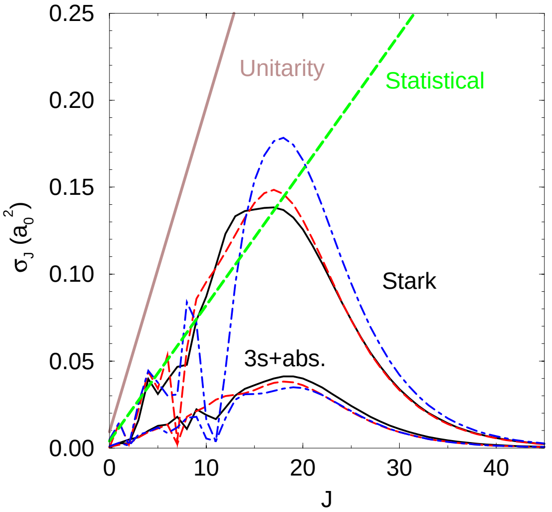

Fig. 14. The average Stark and maximum absorption cross-sections for the $(\pi^-p)_{n=3}+\mathrm{H}$ collisions *vs.* the total angular momentum J at the laboratory kinetic energy $T = 10$ eV. The solid lines are the fully quantum mechanical results, the dashed lines are the semiclassical model, and the dash-dotted lines are the fixed field model. The light solid line is the unitarity limit and the light dashed line corresponds to the assumption of statistical mixing.

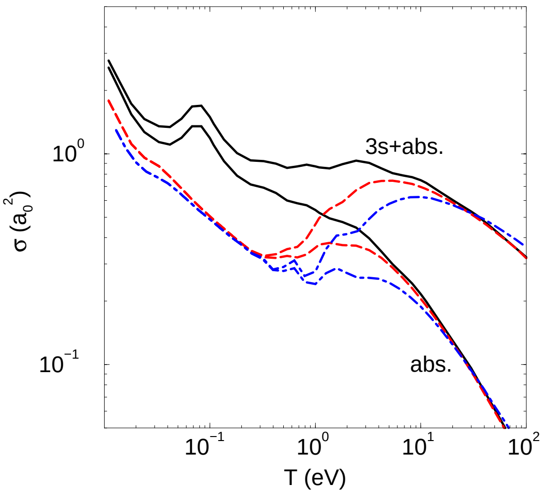

Fig. 15. The energy dependence of the absorption cross-sections, equation (36), and the maximum absorption cross-sections, equation (38), for pionic hydrogen with $n = 3$. The solid lines are the fully quantum mechanical results, the dashed lines are the semiclassical model, and the dash-dotted lines are the fixed field model.

Figure 16 shows the rates for different processes for the $(\pi^-p)_{n=3}$ state in hydrogen gas at a pressure of 15 bar. For energies larger than 0.05 eV Stark mixing is the fastest process while the $3p \to 1s$ radiative transition dominates

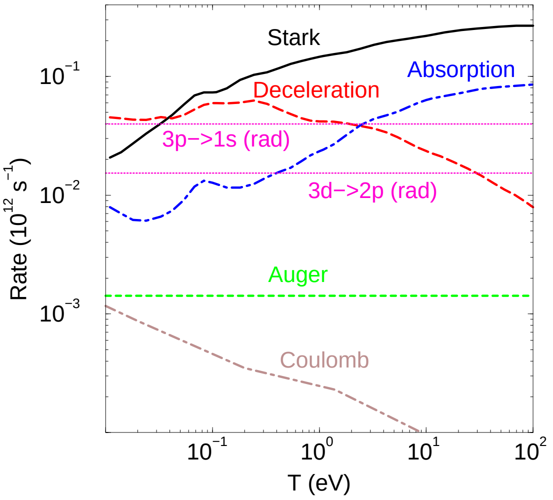

Fig. 16. The energy dependence of the l-average Stark (solid line), deceleration (dashed line), and effective absorption (dash-dotted line) rates for $(\pi^-p)_{n=3}$ at 15 bar. The dotted lines are the radiative $3p \rightarrow 1s$ and $3d \rightarrow 2p$ rates. The light short-dashed line is the $3 \rightarrow 2$ Auger deexcitation rate [1] and the light dash-dotted line is the $3 \rightarrow 2$ adiabatic Coulomb deexcitation rate [31].

for low energies. The effective absorption rate is smaller than the Stark mixing rate due to the low statistical weight of the $3s$ state and the $3p - 3s$ energy difference (only important for low energies). The rates for $3 \rightarrow 2$ adiabatic Coulomb deexcitation [31] and external Auger effect [1] are also shown for comparison; these collisional deexcitation mechanism are obviously suppressed by the absorption[2]. The deceleration rate exceeds the absorption rate below 2 eV, but for higher energies the deceleration is suppressed by the absorption, and for energies above 20 eV becomes insignificant.

4.3 Kaonic hydrogen

The nuclear interaction effects in the scattering of the K^-p atoms in excited states are even more important than in the case of π^-p. The central values of the KEK result for the $1s$ strong interaction shift and width of kaonic hydrogen [33] were used in our calculations:

$$\epsilon_{1s}^{\rm had} = 327 \pm 63({\rm stat}) \pm 11({\rm syst})\ {\rm eV}, \quad (80)$$
$$\Gamma_{1s} = 407 \pm 208({\rm stat}) \pm 100({\rm syst})\ {\rm eV}. \quad (81)$$

The cascade in kaonic hydrogen differs from that of pionic hydrogen in the initial condition, it begins with a higher n level: $n_{\rm init}(K^-p) \sim \sqrt{\mu_{K^-p}} \sim 25$ as compared to $n_{\rm init}(\pi^-p) \sim \sqrt{\mu_{\pi^-p}} \sim 15$. The much larger width of the ns states makes the absorption during the collisions much more probable than in the π^-p atom. Another important difference between the K^-p and π^-p cases is that in K^-p the ns energy shift is repulsive, therefore the $nl \rightarrow ns$ transitions are not allowed below the corresponding threshold. The strong interaction width of the $2p$ state[3] is poorly known from the KN scattering data, but its effect on the collisional rates is negligible.

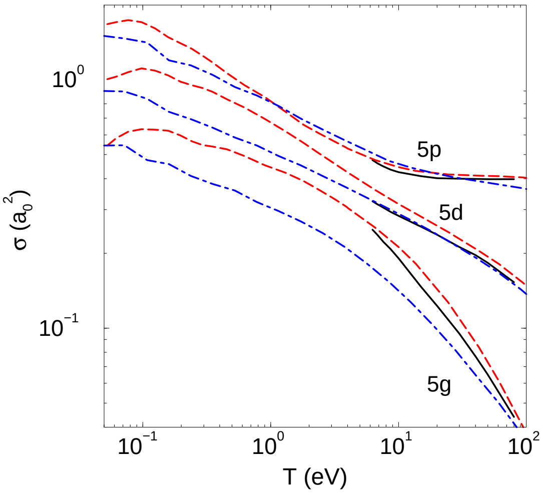

Fig. 17. Absorption cross-sections for K^-p in the $5p$, $5d$, and $5g$ states scattering from hydrogen *vs.* laboratory kinetic energy. The fully quantum mechanical results are shown with solid lines, the semiclassical with dashed lines, and those of the fixed field model with dash-dotted lines.

Figure 17 shows an example of the energy dependence of absorption cross-sections for the states with $n = 5$. The quantum mechanical results are shown only above the $5s$ threshold as our numerical algorithm used in this particular case is not reliable in the presence of closed channels. Overall, there is a fair agreement between the three models above the threshold. The fixed field model does, however, result in absorption cross-sections that are somewhat smaller for $l > 1$ than those of the semiclassical model. This can be explained using Figure 2: the correct angular coupling allows a larger fraction of the substates with $l > 0$ to be mixed with the s state in a single collision and thereby undergo nuclear absorption. Figure 18 shows the l-average Stark, absorption, and deceleration rates for $n = 5$ calculated in the semiclassical model in comparison with the deexcitation rates for a typical gas target at 10 bar. The $(K^-p)_{n=5}$ atoms with high kinetic energies are strongly absorbed while the radiative and Auger deexcitations dominate in the low energy range. Like in the case of pionic hydrogen the situation is complicated by the deceleration due to elastic collisions. The results of cascade calculations based on the presented cross-sections were discussed in [34].

---

[2] There is experimental evidence for the $3 \rightarrow 2$ Coulomb-like deexcitation process in the neutron time-of-flight spectra in both liquid and gaseous (40 bar) hydrogen [32] which can be related to the formation of excited molecular states, see [30] and references therein.

[3] It is important for the cascade calculations and strongly influences the yield of K X-ray lines, see [33,34].

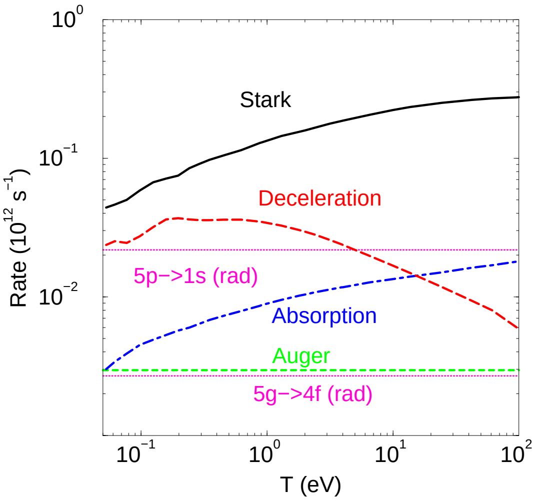

Fig. 18. The energy dependence of the l-average Stark (solid line), absorption (dash-dotted line) and deceleration (dashed line) rates for $(K^-p)_{n=5}$ at 10 bar. The results are calculated in the semiclassical model. The l-average Auger rate [1] is shown with a light dashed line and the radiative rates with dotted lines.

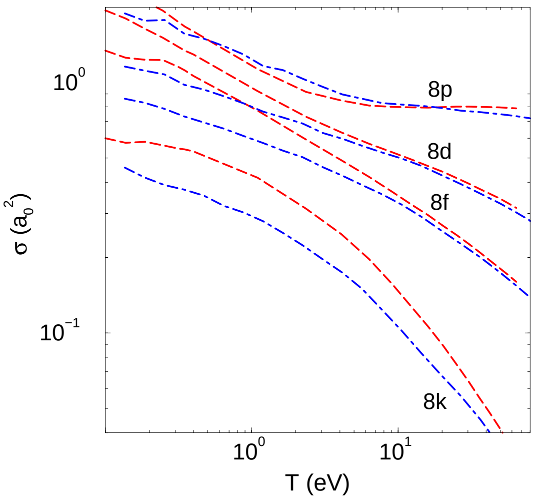

Fig. 19. Absorption cross-sections for $\bar{p}p$ in the $8p$, $8d$, $8f$, and $8k$ states scattering from hydrogen *vs.* laboratory kinetic energy. The results of the semiclassical model are shown with dashed lines, and those of the fixed field model with dash-dotted lines.

4.4 Antiprotonic hydrogen

The case of antiprotonic hydrogen is similar to that of K^-p: the ns nuclear widths are large and the ns nuclear shifts are repulsive. The following values [35] for the spin-averaged shift and width were used in the present calculations:

$$\epsilon_{1s}^{\text{had}} = 721 \pm 14 \text{ eV}, \tag{82}$$

$$\Gamma_{1s} = 1097 \pm 42 \text{ eV}. \tag{83}$$

The hadronic width of the $2p$ state in antiprotonic hydrogen [35]

$$\Gamma_{2p}^{\text{had}} = 32.5 \pm 2.1 \text{ meV} \tag{84}$$

is much larger than the radiative one and absorption during the cascade from the p states is very important. The widths of the other np states are given by

$$\Gamma_{np}^{\text{had}} = \frac{32(n^2-1)}{3n^5}\Gamma_{2p}^{\text{had}}. \tag{85}$$

Figure 19 shows the calculated cross-sections for absorption from the s state at $n = 8$. The energy dependence and the l dependence of these cross-sections are very similar to the kaonic hydrogen case shown in Figure 17. The semiclassical and fixed field models are in a fairly good agreement. As was observed in the K^-p case, the fixed field model underestimates the absorption cross-sections for $l > 1$ due to the approximate treatment of the angular coupling. The rates for the l-average collisional processes for $(\bar{p}p)_{n=8}$ at a pressure of 1 bar are shown in Figure 20 in comparison with the deexcitation rates: here the absorption just begins, it gets more important at the lower n, like in the $(K^-p)_{n=5}$ case shown in Figure 18, and then eventually terminates the cascade. As the $\bar{p}p$ annihilation rate in the $8p$ state is 10^{12} s^{-1}, the p state is almost completely depleted between the collisions at 1 bar. The absorption between collisions from the $8p$ state is comparable in strength to the absorption from the $8s$ state during collisions for energies below 1 eV and about two times stronger for higher energies. The results of detailed cascade calculations for antiprotonic hydrogen will be published elsewhere.

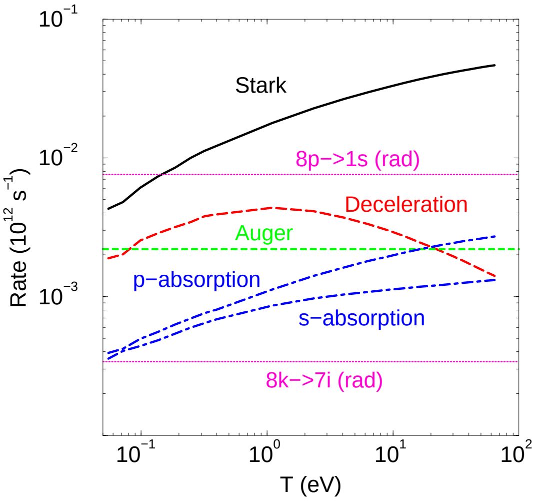

Fig. 20. The energy dependence of the l-average Stark (solid line), effective absorption (dash-dotted lines) and deceleration (dashed line) rates for $\bar{p}p$ for $n = 8$ at 1 bar. The rates are calculated in the semiclassical model. The l-average Auger rate [1] is shown with a light dashed line and the radiative rates with dotted lines.

5 Conclusion

The total and differential cross-sections of Stark mixing and elastic scattering have been calculated for the μ^-p, π^-p, K^-p, and $\bar{p}p$ atoms for the principal quantum numbers and the kinetic energies needed in detailed cascade calculations. For hadronic atoms, the collisional absorption cross-sections have been calculated as well. For the low states $n = 2{-}5$, the calculations have been done in a fully quantum mechanical framework using the close-coupling method. For the first time, the effects of nuclear shifts and width of the ns states have been taken into account straightforwardly in the quantum mechanical scattering problem. For the intermediate states $n = 5{-}10$, the proposed semiclassical model provides an efficient computational method. By treating one degree of freedom (the distance between x^-p and H) classically, one can reduce the original system of the coupled second order equations to a system of first order equations while maintaining the correct angular coupling between the x^-p internal angular momentum and the relative orbital angular momentum of $x^-p + \mathrm{H}$ system. The semiclassical approximation has been found to agree fairly well with the fully quantum mechanical calculations, provided the collisional energy is not too low so that the number of essential partial waves is large. As the threshold behavior is not treated correctly in the semiclassical approximation, transitions to and from the ns states cannot be calculated reliably in the near-threshold region.

Using the above described methods we were able to assess the range of validity of the fixed field model, which was commonly used in many cascade studies. In addition to total Stark mixing and absorption cross-sections calculated with this model in the literature [1,11], we have calculated the differential cross-sections for comparison with the more accurate methods. When compared to the semiclassical model, the fixed field model usually underestimates the absorption cross-sections due to the lack of the rotational coupling among the nl sublevels. When nuclear absorption during collisions is negligible, the fixed field model provides, on average, a fair description in comparison with the semiclassical approximation for kinetic energies larger than a few eV.

The results of this paper have been used in detailed kinetics calculations of atomic cascade in μ^-p and π^-p reported in [23]. The detailed description of the results, together with those in K^-p and $\bar{p}p$, will be published in separate papers [24].

A few problems remain, which are beyond the scope of this paper. First, we have considered collisions with *atomic* hydrogen. One can expect that the molecular structure of the target becomes important for large n states when the characteristic size of the exotic atom cannot be treated as a small parameter in comparison with the conventional atomic scale. We shall address this problem in a separate paper [24]. Molecular effects [30] are also expected to be important at low collisional energy when only a small number of molecular ro-vibrational states can be excited. This kinematical region partly overlaps with the region of small energies where only a few partial waves are important and the dipole approximation is not justified. To deal with these problems a genuine many-body framework is needed.

We thank P. Hauser, F. Kottmann, L. Simons, D. Taqqu, and R. Pohl for fruitful and stimulating discussions.

Appendix A: The rotation functions $\mathbf{D}^{\mathbf{J}}_{\mathbf{\Lambda M}}(\boldsymbol{\alpha}, \boldsymbol{\beta}, \boldsymbol{\gamma})$

This paper uses the conventions of Condon and Shortley for the spherical harmonics and those of reference [36] for the rotation functions $D^J_{\Lambda M}(\alpha, \beta, \gamma)$. The rotation functions $D^J_{M\Lambda}(\alpha, \beta, \gamma)$ are eigenfunctions of the square of the total angular momentum $\mathbf{J}^2$ and its projections J_z and $J_{z'}$ along the z-axis and the z'-axis:

$$\begin{aligned} \mathbf{J}^2 D^J_{M\Lambda}(\alpha, \beta, \gamma) &= J(J+1) D^J_{M\Lambda}(\alpha, \beta, \gamma), \\ J_z D^J_{M\Lambda}(\alpha, \beta, \gamma) &= -M D^J_{M\Lambda}(\alpha, \beta, \gamma), \\ J_{z'} D^J_{M\Lambda}(\alpha, \beta, \gamma) &= -\Lambda D^J_{M\Lambda}(\alpha, \beta, \gamma). \end{aligned} \tag{A.1}$$

The raising and lowering operators are defined by

$$\begin{aligned} J_\pm &= J_x \pm \mathrm{i} J_y, \\ J'_\pm &= J_{x'} \pm \mathrm{i} J_{y'} \end{aligned} \tag{A.2}$$

and have the properties

$$\begin{aligned} J_\pm D^J_{M\Lambda}(\alpha, \beta, \gamma) &= -\lambda_\mp(J, M) D^J_{M\mp 1\Lambda}(\alpha, \beta, \gamma), \\ J'_\pm D^J_{M\Lambda}(\alpha, \beta, \gamma) &= -\lambda_\pm(J, \Lambda) D^J_{M\Lambda\pm 1}(\alpha, \beta, \gamma) \end{aligned} \tag{A.3}$$

where

$$\lambda_\pm(J, M) = \sqrt{J(J+1) - M(M \pm 1)}. \tag{A.4}$$

In this paper only two of the Euler angles, α and β, are used. Therefore, to simplify notation the rotation functions can be written ($\Omega = (\theta, \phi)$):

$$D^J_{M\Lambda}(\Omega) = D^J_{M\Lambda}(\phi, \theta, 0). \tag{A.5}$$

The coefficients $u^{Jl}_{\Lambda L}$ used in the basis transformation (26) can be found using the properties of the rotation functions [36]

$$\begin{aligned} u^{Jl}_{\Lambda L} &= \sqrt{\frac{2J+1}{4\pi}} \\ &\quad \times \int \mathrm{d}\Omega \mathrm{d}\mathbf{r} \Big(D^{J*}_{\Lambda L}(\Omega) \chi_{nl\Lambda}(\mathbf{r}') \Big)^* \mathcal{Y}^{JM}_{Ll}(\Omega, \omega) r_{nl}(r) \\ &= \sum_{M_L m} \Big(\langle L l M_L m | J M \rangle \\ &\quad \times \int \mathrm{d}\Omega \, D^J_{\Lambda M}(\Omega) Y_{L M_L}(\Omega) \int \mathrm{d}\mathbf{r} \chi^*_{nl\Lambda}(\mathbf{r}') \chi_{nlm}(\mathbf{r}) \Big) \\ &= \sum_{M_L m} \Big(\langle L l M_L m | J M \rangle \\ &\quad \times \int \mathrm{d}\Omega \, D^J_{\Lambda M}(\Omega) Y_{L M_L}(\Omega) D^{l*}_{\Lambda m}(\Omega) \Big) \\ &= \sqrt{\frac{2L+1}{2J+1}} \langle L l 0 \Lambda | J \Lambda \rangle \end{aligned} \tag{A.6}$$

for any M with $|M| \leq J$.

Appendix B: Variable phase approach to multichannel scattering

We use a version of the variable phase method (see Ref. [21] and references therein) to compute the scattering matrix. The notation is as follows: ξ is a column vector containing the radial wave functions, K is the diagonal matrix with the channel momenta $K_{mn} = \delta_{mn} k_m$. The angular momentum quantum numbers for the different channels are diagonal elements of the matrix L, *i.e.* $L_{mn} = \delta_{mn} l_m$. Then the radial Schrödinger equation is given by

$$\left(-\frac{\mathrm{d}^2}{\mathrm{d}R^2} + \frac{L(L+1)}{R^2} + W(R) - K^2\right)\xi(R) = 0 \quad \text{(B.1)}$$

where $W(R)$ is the reduced potential matrix.

Let $h_l^{(1)}$ and $h_l^{(2)}$ be Riccati-Hankel functions as defined in reference [21] and H_1 and H_2 diagonal matrices with elements $H_{1mn}(R) = \delta_{mn} h_{l_m}^{(1)}(k_m R)/\sqrt{k_m}$ and $H_{2mn}(R) = \delta_{mn} h_{l_m}^{(2)}(k_m R)/\sqrt{k_m}$.

The scattering matrix $S(R_0)$ obtained from equation (B.1) with W truncated at R_0 (*i.e.* with the substitution $W(R) \rightarrow W(R)\theta(R_0 - R)$) is a function of R_0 and satisfies the equation

$$S' = \frac{\mathrm{i}}{2}(SH_1 - H_2)W(H_1 S - H_2). \quad \text{(B.2)}$$

The scattering matrix of the full problem is given by $S = S(\infty)$.

In equation (B.2) the dependence on the angular momentum is contained in the Riccati-Hankel functions. In numerical calculations, it can be more convenient to combine the potential and the angular momentum term in one effective potential

$$W_{\text{eff}}(R) = W(R) + \frac{L(L+1)}{R^2} \cdot \quad \text{(B.3)}$$

Following the same procedure as in the derivation of equation (B.2) one obtains

$$\bar{S}' = \frac{\mathrm{i}}{2}(\bar{S}\bar{H}_1 - \bar{H}_2)W_{\text{eff}}(\bar{H}_1\bar{S} - \bar{H}_2) \quad \text{(B.4)}$$

where $\bar{H}_1(R) = K^{-1/2}\mathrm{e}^{\mathrm{i}KR}$ and $\bar{H}_2(R) = K^{-1/2}\mathrm{e}^{-\mathrm{i}KR}$. The matrix $\bar{S}(R)$ is related to the scattering matrix by

$$S = \mathrm{e}^{-\mathrm{i}\pi L/2}\bar{S}(\infty)\mathrm{e}^{-\mathrm{i}\pi L/2}. \quad \text{(B.5)}$$

The connection between $S(R)$ and $\bar{S}(R)$ can be established through the identity of the wave functions and their derivatives in R. Let Ξ be a square matrix with linear independent solutions ξ as columns. Ξ and Ξ' can be expressed both in terms of S and $\bar{S}$

$$\begin{aligned} \Xi &= (H_1 S - H_2)N = (\bar{H}_1\bar{S} - \bar{H}_2)\bar{N} \\ \Xi' &= (H_1' S - H_2')N = (\bar{H}_1'\bar{S} - \bar{H}_2')\bar{N} \end{aligned} \quad \text{(B.6)}$$

where N and $\bar{N}$ are square matrices. From the relations (B.6), one finds the following expression for S

$$S = H_1^{-1}\Big((\bar{H}_1\bar{S} - \bar{H}_2)\bar{N}N^{-1} + H_2\Big) \quad \text{(B.7)}$$

with

$$\begin{aligned} \bar{N}N^{-1} = &\Big(H_1'(\bar{H}_1\bar{S} - \bar{H}_2) - H_1(\bar{H}_1'\bar{S} - \bar{H}_2')\Big)^{-1} \\ &\times(H_1 H_2' - H_1' H_2). \end{aligned} \quad \text{(B.8)}$$

We compute the scattering matrix for the $x^- p + H \rightarrow x^- p + H$ process by solving equation (B.4) in the coupled basis with the boundary condition that $\bar{S}(R_{\min})$ is a diagonal matrix with elements

$$\bar{S}_{mn} = \delta_{mn}\frac{1 + \mathrm{i}\tan(k_m R_{\min})}{1 - \mathrm{i}\tan(k_m R_{\min})} \quad \text{(B.9)}$$

which is the scattering matrix for S-wave scattering from an infinitely hard sphere with radius $R_{\min}$. The effect of nuclear absorption from the ns states is included by adding the imaginary part (the real part is already taken into account in the momentum matrix K) of the ns energy shift to the potential

$$\begin{aligned} W_{ij}(R) = 2\mu\Big(&\langle n; L'l'JM|V(R)|n; LlJM\rangle \\ &+\delta_{l0}\delta_{l'0}(-\mathrm{i}\Gamma_{ns}/2)\theta(R_0 - R)\Big)\cdot \end{aligned} \quad \text{(B.10)}$$

The nuclear absorption is turned off for distances larger than R_0; we use $R_0 = 5a_0$ in this paper. This allows the mixing $nl \leftrightarrow ns$ to take place during the collision together with the absorption effects while the ns states remain well defined asymptotic states.

It is necessary to set the boundary condition away from $R = 0$ because the potential taken in the dipole approximation has an R^{-2} singularity at $R = 0$, which makes the Schrödinger equation ill-defined. Throughout this paper we use the value $R_{\min} = 0.05a_0$ unless otherwise stated.

References

1. M. Leon, H.A. Bethe, Phys. Rev. **127**, 636 (1962).
2. E. Borie, M. Leon, Phys. Rev. A **21**, 1460 (1980).
3. V.E. Markushin, Phys. Rev. A **50**, 1137 (1994).
4. V.E. Markushin, Hyperf. Interact. **119**, 11 (1999).
5. D. Taqqu *et al.*, Hyperf. Interact. **119**, 311 (1999).
6. D. Gotta, Newsletter **15**, 276 (1999).
7. D. Gotta *et al.*, Nucl. Phys. A **660**, 283 (1999).
8. J.-L. Vermeulen, Nucl. Phys. B **12**, 506 (1969).
9. G. Kodosky, M. Leon, Nuovo Cimento B **1**, 41 (1971).
10. M.C. Struensee, J.S. Cohen, Phys. Rev. A **38**, 44 (1988).
11. T.P. Terada, R.S. Hayano, Phys. Rev. C **55**, 73 (1997).
12. V.P. Popov, V.N. Pomerantsev, Hyperf. Interact. **101/102**, 133 (1996).
13. V.P. Popov, V.N. Pomerantsev, Hyperf. Interact. **119**, 133 (1999).
14. V.P. Popov, V.N. Pomerantsev, Hyperf. Interact. **119**, 137 (1999).

15. V.V. Gusev, V.P. Popov, V.N. Pomerantsev, Hyperf. Interact. **119**, 141 (1999).
16. G. Carboni, G. Fiorentini, Nuovo Cimento B **39**, 281 (1977).
17. T.S. Jensen, V.E. Markushin, PSI-PR-99-32 (1999), `nucl-th/0001009`.
18. T.S. Jensen, V.E. Markushin, Nucl. Phys. A **689**, 537 (2001).
19. S. Deser *et al.*, Phys. Rev. **96**, 774 (1954).
20. R.T. Pack, J.O. Hirschfelder, J. Chem. Phys. **49**, 4009 (1968).
21. F. Calogero, *Variable Phase Approach to Potential Scattering* (Academic Press, New York, 1967).
22. C.J. Joachain, *Quantum Collision Theory* (North-Holland Publishing Company, Amsterdam, 1975).
23. V.E. Markushin, T.S. Jensen, Hyperf. Interact. (in press).
24. T.S. Jensen, V.E. Markushin, (to be published); T.S. Jensen, thesis, University of Zürich, 2002.
25. L.I. Ponomarev, E.A. Solov'ev, Hyperf. Interact. **119**, 55 (1999).
26. G. Reifenröther *et al.*, Phys. Lett. B **214**, 325 (1988).
27. G. Reifenröther, E. Klempt, Nucl. Phys. A **503**, 885 (1989).
28. H.-Ch. Schroeder *et al.*, Phys. Lett. B **469**, 25 (1999).
29. H.-Ch. Schroeder *et al.*, Eur. Phys. J. C **21**, 473 (2001).
30. S. Jonsell, J. Wallenius, P. Froelich, Phys. Rev. A **59**, 3440 (1999).
31. L.I. Ponomarev, E.A. Solov'ev, JETP Lett. **64**, 135 (1999).
32. J. Schottmüller *et al.*, Hyperf. Interact. **119**, 95 (1999).
33. M. Iwasaki *et al.*, Phys. Rev. Lett. **78**, 3067 (1997).
34. V.E. Markushin, T.S. Jensen, Nucl. Phys. A **691**, 318 (2001).
35. M. Augsburger *et al.*, Nucl. Phys. A **658**, 149 (1999).
36. D.A. Varshalovich, A.N. Moskalev, V.K. Khersonskii, *Quantum Theory of Angular Momentum* (World Scientific Publishing Co Ptc. Ltd., Singapore, 1988).